Highly sensitive multi-core flat fiber surface plasmon resonance refractive index sensor

Ahmmed A. Rifat,[1] G. A. Mahdiraji,[1,2] Yong Meng Sua,[1] Rajib Ahmed,[3] Y. G. Shee,[1] and F. R. Mahamd Adikan[1,2,*]

[1]*Integrated Lightwave Research Group, Department of Electrical Engineering, Faculty of Engineering, University of Malaya, Kuala Lumpur-50603, Malaysia*
[2]*Flexilicate Sdn Bhd, University of Malaya, Kuala Lumpur-50603, Malaysia*
[3]*Nanotechnology Laboratory, School of Mechanical Engineering, University of Birmingham, Birmingham B15 2TT, UK*
[*]*rafiq@um.edu.my*

Abstract: A simple multi-core flat fiber (MCFF) based surface plasmon resonance (SPR) sensor operating in telecommunication wavelengths is proposed for refractive index sensing. Chemically stable gold (Au) and titanium dioxide (TiO_2) layers are used outside the fiber structure to realize a simple detection mechanism. The modeled sensor shows average wavelength interrogation sensitivity of 9,600 nm/RIU (Refractive Index Unit) and maximum sensitivity of 23,000 nm/RIU in the sensing range of 1.46-1.485 and 1.47-1.475, respectively. Moreover, the refractive index resolution of 4.35×10^{-6} is demonstrated. Additionally, proposed sensor had shown the maximum amplitude interrogation sensitivity of 820 RIU^{-1}, with the sensor resolution of 1.22×10^{-5} RIU. To the best of our knowledge, the proposed sensor achieved the highest wavelength interrogation sensitivity among the reported fiber based SPR sensors. Finally we anticipate that, this novel and highly sensitive MCFF SPR sensor will find the potential applications in real time remote sensing and monitoring, ultimately enabling inexpensive and accurate chemical and biochemical analytes detection.

OCIS codes: (240.6680) Surface plasmons; (060.5295) Photonic crystal fibers; (060.2370) Fiber optics sensors; (280.4788) Optical sensing and sensors.

References and links

1. B. Lee, S. Roh, and J. Park, "Current status of micro-and nano-structured optical fiber sensors," Opt. Fiber Technol. **15**(3), 209–221 (2009).
2. B. Gupta and R. Verma, "Surface plasmon resonance-based fiber optic sensors: principle, probe designs, and some applications," J. Sens. **2009**, 979761 (2009).
3. B. Liedberg, C. Nylander, and I. Lunström, "Surface plasmon resonance for gas detection and biosensing," Sens. Actuators **4**, 299–304 (1983).
4. G. Robinson, "The commercial development of planar optical biosensors," Sensor Actuat. Biol. Chem. **29**, 31–36 (1995).
5. A. Hassani, B. Gauvreau, M. F. Fehri, A. Kabashin, and M. Skorobogatiy, "Photonic crystal fiber and waveguide-based surface plasmon resonance sensors for application in the visible and near-IR," Electromagnetics **28**(3), 198–213 (2008).
6. Y. Rao and T. Zhu, "A highly sensitive fiber-optic refractive index sensor based on an edge-written long-period fiber grating," in *Nonlinear Photonics*, OSA Technical Digest (CD) (Optical Society of America, 2007), paper JWA53.
7. Y. Zhao, X.-G. Li, L. Cai, and Y. Yang, "Refractive index sensing based on photonic crystal fiber interferometer structure with up-tapered joints," Sensor Actuat. Biol. Chem. **221**, 406–410 (2015).
8. A. Iadicicco, A. Cusano, A. Cutolo, R. Bernini, and M. Giordano, "Thinned fiber Bragg gratings as high sensitivity refractive index sensor," IEEE Photonics Technol. Lett. **16**(4), 1149–1151 (2004).
9. R. Ahmed, A. A. Rifat, A. K. Yetisen, S. H. Yun, S. Khan, and H. Butt, "Mode-multiplexed waveguide sensor," J. Electromagn. Wave, in press.
10. Y. Zhao, L. Cai, X.-G. Li, F.-c. Meng, and Z. Zhao, "Investigation of the high sensitivity RI sensor based on SMS fiber structure," Sensor Actuat. A-Phys. **205**, 186–190 (2014).

#252520 Received 22 Oct 2015; revised 8 Dec 2015; accepted 22 Dec 2015; published 29 Jan 2016

11. R. Jorgenson and S. Yee, "A fiber-optic chemical sensor based on surface plasmon resonance," Sensor Actuat. Biol. Chem. **12**, 213–220 (1993).
12. Y. Zhao, Z.-q. Deng, and J. Li, "Photonic crystal fiber based surface plasmon resonance chemical sensors," Sensor Actuat. Biol. Chem. **202**, 557–567 (2014).
13. Z. Tan, X. Li, Y. Chen, and P. Fan, "Improving the sensitivity of fiber surface plasmon resonance sensor by filling liquid in a hollow core photonic crystal fiber," Plasmonics **9**(1), 167–173 (2014).
14. B. Shuai, L. Xia, and D. Liu, "Coexistence of positive and negative refractive index sensitivity in the liquid-core photonic crystal fiber based plasmonic sensor," Opt. Express **20**(23), 25858–25866 (2012).
15. D. Gao, C. Guan, Y. Wen, X. Zhong, and L. Yuan, "Multi-hole fiber based surface plasmon resonance sensor operated at near-infrared wavelengths," Opt. Commun. **313**, 94–98 (2014).
16. J. N. Dash and R. Jha, "SPR biosensor based on polymer pcf coated with conducting metal oxide," IEEE Photonics Technol. Lett. **26**(6), 595–598 (2014).
17. A. A. Rifat, G. A. Mahdiraji, D. M. Chow, Y. G. Shee, R. Ahmed, and F. R. Adikan, "Photonic crystal fiber-based surface plasmon resonance sensor with selective analyte channels and graphene-silver deposited core," Sensors (Basel) **15**(5), 11499–11510 (2015).
18. P. J. Sazio, A. Amezcua-Correa, C. E. Finlayson, J. R. Hayes, T. J. Scheidemantel, N. F. Baril, B. R. Jackson, D.-J. Won, F. Zhang, E. R. Margine, V. Gopalan, V. H. Crespi, and J. V. Badding, "Microstructured optical fibers as high-pressure microfluidic reactors," Science **311**(5767), 1583–1586 (2006).
19. J. N. Dash and R. Jha, "On the performance of graphene-based D-shaped photonic crystal fibre biosensor using surface plasmon resonance," Plasmonics **10**(5), 1123–1131 (2015).
20. M. Tian, P. Lu, L. Chen, C. Lv, and D. Liu, "All-solid D-shaped photonic fiber sensor based on surface plasmon resonance," Opt. Commun. **285**(6), 1550–1554 (2012).
21. J. N. Dash and R. Jha, "Graphene based birefringent photonic crystal fiber sensor using surface plasmon resonance," IEEE Photon. Technol. Lett. **26**(11), 1092–1095 (2014).
22. R. Otupiri, E. Akowuah, S. Haxha, H. Ademgil, F. AbdelMalek, and A. Aggoun, "A novel birefrigent photonic crystal fibre surface plasmon resonance biosensor," IEEE Photon. J. **6**(4), 1–11 (2014).
23. E. K. Akowuah, T. Gorman, H. Ademgil, S. Haxha, G. K. Robinson, and J. V. Oliver, "Numerical analysis of a photonic crystal fiber for biosensing applications," IEEE J. Quantum Electron. **48**(11), 1403–1410 (2012).
24. A. A. Rifat, G. A. Mahdiraji, Y. M. Sua, Y. G. Shee, R. Ahmed, D. M. Chow, and F. R. M. Adikan, "Surface plasmon resonance photonic crystal fiber biosensor: a practical sensing approach," IEEE Photon. Technol. Lett. **27**(15), 1628–1631 (2015).
25. A. A. Rifat, G. A. Mahdiraji, R. Ahmed, D. M. Chow, Y. M. Sua, Y. G. Shee, and F. R. M. Adikan, "Copper-graphene based photonic crystal fiber plasmonic biosensor," IEEE Photon. J. in press.
26. A. A. Rifat, G. A. Mahdiraji, Y. G. Shee, M. J. Shawon, and F. R. M. Adikan, "A novel photonic crystal fiber biosensor based on surface plasmon resonance," Procedia Eng. in press.
27. F. R. M. Adikan, S. R. Sandoghchi, C. W. Yi, R. E. Simpson, M. A. Mahdi, A. S. Webb, J. C. Gates, and C. Holmes, "Direct UV written optical waveguides in flexible glass flat fiber chips," IEEE J. Sel. Top. Quantum Electron. **18**(5), 1534–1539 (2012).
28. C. Holmes, F. R. Mahamd Adikan, A. S. Webb, J. C. Gates, C. B. E. Gawith, J. K. Sahu, P. G. R. Smith, and D. N. Payne, "Evanescent field sensing in novel flat fiber," in *Conference on Lasers and Electro-Optics/Quantum Electronics and Laser Science Conference and Photonic Applications Systems Technologies*, OSA Technical Digest (CD) (Optical Society of America, 2008), paper CMJJ3.
29. O. N. Egorova, S. L. Semjonov, A. K. Senatorov, M. Y. Salganskii, A. V. Koklyushkin, V. N. Nazarov, A. E. Korolev, D. V. Kuksenkov, M.-J. Li, and E. M. Dianov, "Multicore fiber with rectangular cross-section," Opt. Lett. **39**(7), 2168–2170 (2014).
30. G. A. Mahdiraji, F. Amirkhan, D. M. Chow, Z. Kakaie, P. S. Yong, K. D. Dambul, and F. R. M. Adikan, "Multicore flat fiber: a new fabrication technique," IEEE Photonics Technol. Lett. **26**(19), 1972–1974 (2014).
31. G. A. Mahdiraji, "Low-crosstalk semi-trench-assisted multicore flat fiber," in *Optical Fiber Communication Conference*, OSA Technical Digest (online) (Optical Society of America, 2015), paper W2A.32.
32. G. Amouzad Mahdiraji, D. M. Chow, S. Sandoghchi, F. Amirkhan, E. Dermosesian, K. S. Yeo, Z. Kakaei, M. Ghomeishi, S. Y. Poh, S. Yu Gang, and F. R. Mahamd Adikan, "Challenges and solutions in fabrication of silica-based photonic crystal fibers: an experimental study," Fiber Int. Opt. **33**(1-2), 85–104 (2014).
33. P. Malinský, P. Slepička, V. Hnatowicz, and V. Svorčík, "Early stages of growth of gold layers sputter deposited on glass and silicon substrates," Nanoscale Res. Lett. **7**(1), 241 (2012).
34. M. Vieweg, T. Gissibl, S. Pricking, B. T. Kuhlmey, D. C. Wu, B. J. Eggleton, and H. Giessen, "Ultrafast nonlinear optofluidics in selectively liquid-filled photonic crystal fibers," Opt. Express **18**(24), 25232–25240 (2010).
35. B. T. Kuhlmey, B. J. Eggleton, and D. K. Wu, "Fluid-filled solid-core photonic bandgap fibers," J. Lightwave Technol. **27**(11), 1617–1630 (2009).
36. W. Qin, S. Li, Y. Yao, X. Xin, and J. Xue, "Analyte-filled core self-calibration microstructured optical fiber based plasmonic sensor for detecting high refractive index aqueous analyte," Opt. Lasers Eng. **58**, 1–8 (2014).
37. P. R. West, S. Ishii, G. V. Naik, N. K. Emani, V. M. Shalaev, and A. Boltasseva, "Searching for better plasmonic materials," Laser Photon. Rev. **4**(6), 795–808 (2010).
38. A. Vial, A.-S. Grimault, D. Macías, D. Barchiesi, and M. L. de la Chapelle, "Improved analytical fit of gold dispersion: Application to the modeling of extinction spectra with a finite-difference time-domain method," Phys. Rev. B **71**(8), 085416 (2005).
39. J. R. DeVore, "Refractive indices of rutile and sphalerite," J. Opt. Soc. Am. A **41**(6), 416–417 (1951).

#252520 Received 22 Oct 2015; revised 8 Dec 2015; accepted 22 Dec 2015; published 29 Jan 2016

40. A. Hassani and M. Skorobogatiy, "Design of the microstructured optical fiber-based surface plasmon resonance sensors with enhanced microfluidics," Opt. Express **14**(24), 11616–11621 (2006).
41. B. Gauvreau, A. Hassani, M. Fassi Fehri, A. Kabashin, and M. A. Skorobogatiy, "Photonic bandgap fiber-based Surface Plasmon Resonance sensors," Opt. Express **15**(18), 11413–11426 (2007).

1. Introduction

Surface plasmon resonance (SPR) sensor has attracted much attention since the last few decades because of its wide range of applications and high sensitive nature. SPR sensor has several potential applications such as organic-chemical detection, medical diagnostics, biological analyte detection, food quality control, environmental protection, etc [1]. Generally, prism coupling geometry is used to introduce the SPR phenomenon where prism is coated with plasmonic materials (Au, Ag, Cu, etc.) and the incident transverse magnetic (TM) or p-polarization light propagates through the prism to the metal-dielectric interface [2]. When the frequency of incident photons and the frequency of the surface electrons are matched, the incident light will excite the free electrons of the metal surface and resulting surface plasmon wave (SPW) that is generated along the metal surface. Liedberg *et al.* first reported the prism SPR technique for the bio-sensing and gas detection in 1983 [3]. Prism SPR technique is simple in terms of fabrication because of its planar structure, where metal layers can be incorporated easily. Although the prism based SPR sensor (Kretschmann set-up) performance is robust, but its structural configuration is bulky due to optical and mechanical components which is not suitable for remote sensing [4, 5].

To miniaturize the sensor size and cost effective, fiber-based SPR sensors were explored for its feasibilities in sensing. By harnessing the advantages of photonic crystal fiber (PCF) such as small-size, design flexibility and birefringence; manipulation of evanescent field and maintaining light propagation in single mode is possible. Furthermore, increasing the sensitivity and enhancing the sensing range are possible by optimizing the PCFs parameters. Besides the PCF SPR sensor, there are different type of fiber or waveguide based refractive index (RI) sensing techniques such as long period fiber grating (LPFG), fiber Bragg grating (FBG), modal interferometer and micro-ring resonator based sensing [6–10]. The main limitation of these sensors are the low sensitivity, where a very small wavelength shift occur against the changes in analyte's refractive index (RI). Unlike, SPR sensor shows a large resonance wavelength shift due to even a small change of analyte's RI, resulting the high sensitivity is observed. This high sensitivity leads to the high analyte detection accuracy. Since the first demonstration of optical fiber SPR sensor in 1993 by Jorgenson [11], numerous of PCF SPR sensors have been reported for improving the sensor performance with reduced structural complexity [12, 13]. Various PCF SPR sensors, where metals are coated and liquid infiltrated selectively inside the holes have been reported [14–17]. Homogeneous deposition of metals inside the selective PCF holes are challenging. High pressure chemical deposition technique is proposed to homogenously coat the metal layers inside the surface of fiber holes [18]. To overcome the metal coating problems, D-shaped PCF SPR sensors have been proposed [13, 19, 20], where upper part of PCF is polished and the metal layer applied on the flat top. However, this requires accurate polishing effort to precisely remove a predetermined portion of the PCF. In recent times, several PCF SPR biosensors has been reported where the metallic layer and sensing layer are located outside the PCF structure for the purpose of ease sensing [21–26]. However, fabrication of such irregular PCF structures that requires different sizes of holes to be placed in specific positions in the fiber geometry would be practically challenging even with very accurate fiber preform drilling systems. Thus, a simpler and scalable structure will lead to feasible solution for ubiquitous remote SPR sensing.

Optical fibers are potential candidate for the distributed or remote base optical sensing as they are mechanically flexible, immune to electromagnetic interference (EMI), low loss in telecom wavelengths and can be fabricated over kilometer-lengths. On the other hand, planar lightwave circuits offer multifunctionality with the capability to sense multiple substances on a single platform. Flat optical fiber is a hybrid format of waveguide that combines the advantages of conventional optical fiber with the multifunctionality of planar waveguides [27, 28]. Recently, Egorova *et. al*. [29] and Ghafour *et al.* [30, 31] fabricated a new type of flat

#252520 Received 22 Oct 2015; revised 8 Dec 2015; accepted 22 Dec 2015; published 29 Jan 2016

fiber, namely multi-core flat fiber (MCFF), which opens a new window for designing more versatile photonic sensors due to larger and flat surface functionality and flexibility in employing multiple waveguide channels with similar or different operating wavelengths.

In this study, a novel, highly sensitive MCFF structure based SPR sensor is numerically demonstrated for the first time. Metallic layer and sensing layer are placed outside the fiber structure which made the proposed sensor simpler in terms of fabrication. The proposed sensor can be fabricated by following the MCFF method [30, 32] and thin layer deposition by sputtering method [33]. Besides, selective liquid infiltration of holes in PCF can be done by closing the dedicated holes using two-photon direct laser writing [34] and direct gluing method [35]. Since a very short length of optical fiber is required for SPR sensors, the insertion and exchange of liquid inside the fiber holes are practically feasible. The detection of analyte can be carried out simply by flowing it through or dripped on the outer surface of metal layer. The proposed sensor can be calibrated with a liquid with known RI, using the flow cell analyte containing process. The effect of sensor structural parameters such as gold thickness, titanium dioxide thickness and core diameter on the plasmonic excitation is analyzed and optimized for the sensing performance as well as reducing the sensor footprint.

2. MCFF SPR sensor design and theoretical modeling

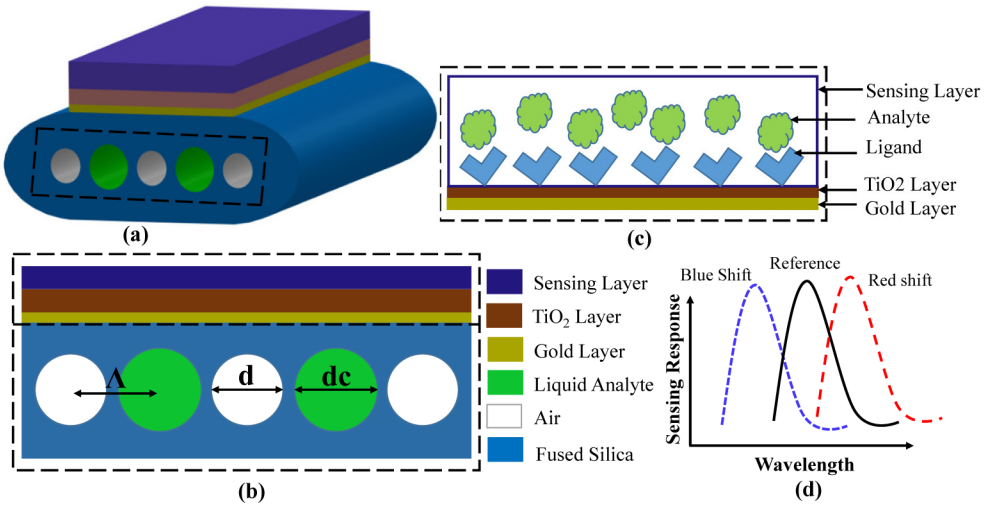

Fig. 1. (a) Schematic diagram of the proposed MCFF sensor in 3D model, (b) Cross-section of 2D computational model of MCFF SPR sensor, (c) Analyte flow through sensing layer: Ligands attached with TiO_2 layer, (d) Sensing response curve: reference peak (without analyte presence), shift right (red) or left (blue) with the presence of analytes.

Figure 1(a) shows the schematic diagram of the proposed MCFF sensor where the identical liquid cores and air-holes are arranged in a line. The proposed sensor is consists of five air-holes where two of them are filled with the high refractive index liquid to fulfill the total internal reflection condition for light guiding. The air hole is filled with high refractive index liquids in alternating sequence in order to optimize the evanescent field, which in turn improve the sensitivity of the sensor. To simplify the fabrication process, gold layer, titanium dioxide layer and sensing layer are arranged sequentially on top of the MCFF surface, as shown in Fig. 1(b). Figure 1(c) is a magnified diagram where analyte will flow through the sensing medium and bond with the ligands, resulting the shift in resonance peak. Due to the presence of analyte, resonance peak can be either blue or red shifted as shown in Fig. 1(d) [14, 36]. A higher refractive index liquid analyte (varies RI from 1.460 to 1.485) is used in the cores compared to the silica (SiO_2) to allow the total internal reflection (TIR) guiding mechanism. The proposed sensor has a pitch size of Λ = 1.20 µm, core diameter d_c = 1.20 µm and the air hole diameter is d = 1 µm. Generally, gold (Au) and silver (Ag) are widely used

#252520 Received 22 Oct 2015; revised 8 Dec 2015; accepted 22 Dec 2015; published 29 Jan 2016

for the plasmonic applications due to their relatively low loss in the visible and near-infrared region (NIR) [37]. Although, silver has low loss in the visible range, it is chemically unstable and it oxidizes easily. Gold is used as the active plasmonic material which is chemically stable and also having the higher resonance shift capability [16]. On top of the gold layer, a thin transparent high refractive index TiO_2 layer is deposited. The presence of TiO_2 layer will enhance the interaction of evanescent field with the analyte layer and shifted the resonant wavelengths towards the near-infrared wavelengths. Recently, Di Gao *et al.* reported the multi-hole based SPR sensor with TiO_2 layer to operate at near-infrared region [15]. Gold layer is used outside the cladding with the fixed thickness, t_g = 40 nm and a TiO_2 layer above the gold layer with thickness, t = 80 nm. Sequentially, sensing layer is on top of the TiO_2 surface. The refractive index of the fused silica is obtained by following the Sellmeier equation [23].

$$n^2(\lambda) = 1 + \frac{B_1\lambda^2}{\lambda^2 - C_1} - \frac{B_2\lambda^2}{\lambda^2 - C_2} - \frac{B_3\lambda^2}{\lambda^2 - C_3} \tag{1}$$

where refractive index of the silica is n and wavelength, λ is in micron. Moreover, Sellmeier coefficient are B_1 = 0.69616300, B_2 = 0.407942600, B_3 = 0.897479400, C_1 = 4.67914826 × 10^{-3} μm^2, C_2 = 1.35120631 × 10^{-2} μm^2 and C_3 = 97.9340025 μm^2.

The dielectric constant of gold is defined by the Drude-Lorentz model [38] and the equation is written as:

$$\varepsilon_{Au} = \varepsilon_\infty - \frac{\omega_D^2}{\omega(\omega + j\gamma_D)} - \frac{\Delta\varepsilon.\Omega_L^2}{(\omega^2 - \Omega_L^2) + j\Gamma_L\omega} \tag{2}$$

where ε_{Au} is the permittivity of dielectric material (gold), ε_∞ is the permittivity at high frequency and its value is 5.9673. The angular frequency can be expressed as $\omega = 2\pi c/\lambda$, c is the velocity of light in vacuum. Moreover, ω_D and γ_D are the plasma frequency and damping frequency respectively, whereas $\Omega_D/2\pi$ = 2113.6 THz and $\gamma_D/2\pi$ = 15.92 THz. Weighting factor is expressed as $\Delta\varepsilon$ = 1.09 while, $\Gamma_L/2\pi$ = 104.86 THz and $\Omega_L/2\pi$ = 650.07 THz are the spectral width and oscillator strength respectively of the Lorentz oscillators.

The refractive index profile of TiO_2 is calculated by the following equation [39].

$$n^2 = 5.913 + \frac{2.441\times10^7}{(\lambda^2 - 0.803\times10^7)} \tag{3}$$

Finite-element method (FEM) based commercial COMSOL software is used to investigate the guiding properties and sensing performance of the proposed sensor. Outside the structure, perfectly matched layer (PML) and scattering boundary conditions are sequentially used to absorb the radiated light towards the surface. Convergence test also carried out by optimizing the mesh size and PML thickness, which leads to calculate the accurate results. The computational area is meshed by the triangular domain elements and boundary elements with 12,822 and 894, respectively; and the maximum number of degrees of freedom equals 90,331.

3. Results and discussion of the MCFF-SPR sensor

PCF SPR sensors operation are based on the evanescent fields and it's interact with the analytes. The core-cladding arrangement in a line leads to leakage of light that produces more evanescent fields. By keeping the metallic layer close to the cores which help to excite free electrons of the metal layer easily, and hence introducing surface plasmon. At a certain wavelength, real effective index (n_{eff}) value of core-guided mode and real n_{eff} of surface plasmon polaritons (SPP) mode is equal, this wavelength is called the resonant wavelength. At the resonant wavelength, evanescent field can easily excite the free electrons of metal surface, resulting the generation of surface plasmon waves (SPWs). The proposed design

#252520 Received 22 Oct 2015; revised 8 Dec 2015; accepted 22 Dec 2015; published 29 Jan 2016

shows two fundamental modes (x- and y-component modes), in this work y-component fundamental mode is analyzed to investigate the propagation loss. The x-component fundamental mode shows the same resonance peak similar to y-component but with lower loss depth. The fundamental core guided mode, SPP mode and the resonant spectrum at analyte refractive index (RI) n_a = 1.46 is shown in Fig. 2. The real part of n_{eff} of the core guided mode and the SPP mode are presented by the green and red solid line respectively. The effective index of the core-guided fundamental mode (green) and SPP mode (red) coincide at resonant wavelength of 1.345 μm, where a sharp loss peak is found. This indicates the maximum energy transfer from the core-guided fundamental mode to the SPP mode. By using the imaginary part of n_{eff}, the propagation loss is defined by the following equation [23].

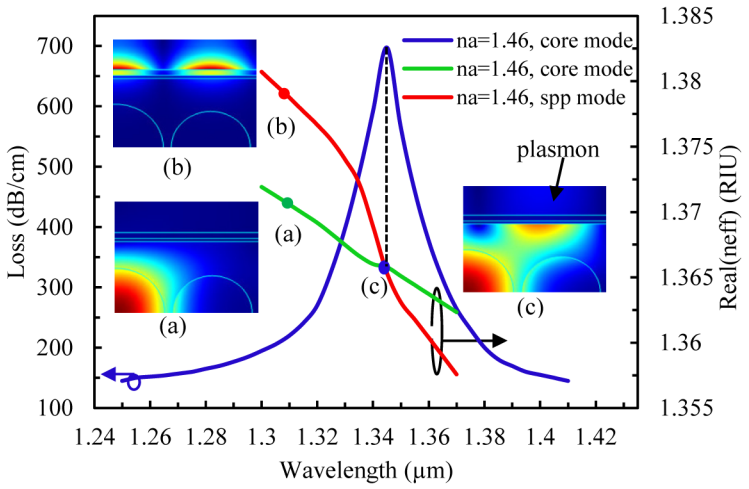

Fig. 2. Dispersion relations of the plasmonic mode (red), fundamental core mode (green), and loss spectra (blue) with the structural parameters: d_c = 1.20 μm, d = 1 μm, t = 40 nm, t_t = 80 nm.

$$\alpha = 40\pi.Im\left(n_{eff}\right)/\left(ln(10)\lambda\right) \approx 8.686 \times k_0.Im\left[n_{eff}\right] \times 10^4\, dB/cm \qquad (4)$$

where $k_0 = 2\pi/\lambda$ is the wave number in the free space and the wavelength, λ is in micron.

It is clearly visible from inset (a) that at the core guided fundamental mode, the electric field is well confined in the liquid core and the SPP mode, and from inset (b), the electric field is introduced on the metal surface outside the resonant wavelength. In inset (c), the fundamental core mode and SPP mode are phase matched at wavelength 1.345 μm. At this wavelength, the fundamental mode and the SPP mode are coupled together. A sharp loss peak appears at phase matching wavelength, providing a signature for detection of the analyte. The performance of proposed sensor is evaluated in terms of sensitivity, accuracy, linearity and resolution. The proposed sensor is very sensitive due to small change of analyte. The small change of analyte RI induces a significant shift of loss peak. Figure 3 shows the response of the sensor for analyte RI from 1.46 to 1.485.

#252520 Received 22 Oct 2015; revised 8 Dec 2015; accepted 22 Dec 2015; published 29 Jan 2016

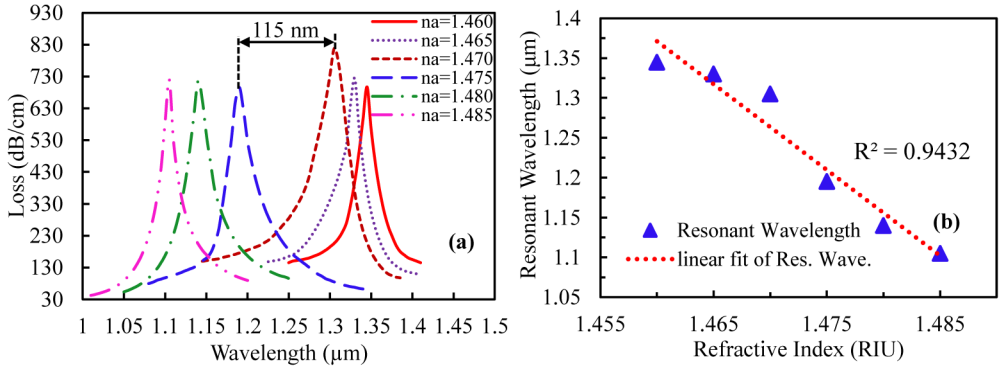

Fig. 3. (a) Loss spectrum with varying analyte RI (n_a) from 1.46 to 1.485; (b) linear fitting of the fundamental mode resonant wavelength vs. analyte RI.

The real part of n_{eff} of plasmonic mode depends strongly on the vicinity layer of analyte RI. Due to the small change of analyte RI, real part of the n_{eff} of SPP mode changes, which causes the change of phase matching wavelength between the cores guided mode and the SPP mode. As depicted in Fig. 3(a), by increasing the analyte RI, the loss peak shifts toward the shorter wavelengths, which is in agreement with the works reported in [14, 36]. The increase in analyte RI will affect the Re(n_{eff}) of both fundamental and SPP mode. In fact, due to presence of strong evanescent field, the increment of Re(n_{eff}) value of fundamental mode is larger compared to the Re(n_{eff}) of SPP mode, resulting in blue shift of the resonance peak [14, 36]. As a result, the phase matching wavelength or resonance peak is shifted towards the lower wavelength. By varying the analyte RI with an iteration of 0.005, resonance wavelength shifts are 15, 25, 115, 50 and 35 nm, respectively towards the lower wavelength, as shown in Table 1. The highest sensitivity is observed within the analyte RI of 1.47 to 1.475, which provides the maximum loss peak shift 115 nm, i.e., from 1.305 to 1.190 μm. Moreover, the maximum and minimum loss peak values 818 and 695 dB/cm are achieved at 1.305 and 1.190 μm wavelength while the analyte RI are 1.47 and 1.475, respectively. Generally, microstructured optical fiber based SPR sensors show high propagation loss, and hence limits the sensor length to generate the measurable signal [40]. The sensitivity of the proposed sensor is analyzed by using the wavelength interrogation and amplitude interrogation method. The sensitivity of wavelength interrogation is measured by the following equation [17],

$$Sensitivity, S_{\lambda[nm/RIU]} = \Delta\lambda_{peak} / \Delta n_a \quad (5)$$

where $\Delta\lambda_{peak}$ is the resonance peak shift and Δn_a is the variation of the analyte refractive index.

Table 1. Performance analysis with the variation of analyte RI.

Analyte RI	Resonance peak wavelength (μm)	Resonance peak shift (nm)	Sensitivity [nm/RIU]	FWHM (nm)
1.460	1.345	15	3000	36
1.465	1.330	25	5000	43
1.470	1.305	115	23000	54
1.475	1.190	50	10000	46
1.480	1.140	35	7000	41
1.485	1.105	-	-	29

The proposed MCFF sensor shows the maximum sensitivity of 23000 nm/RIU, at the analyte RI of 1.47 and the average sensitivity of the sensor is 9600 nm/RIU. The resonance peaks are found at wavelengths of 1.345, 1.330, 1.305, 1.190, 1.140 and 1.105 μm where the full-width-at-half-maximum (FWHM) values are 36, 43, 54, 46, 41 and 29 nm for the analyte refractive index 1.46, 1.465, 1.47, 1.475, 1.48 and 1.485, respectively, as shown in Table 1.

#252520 Received 22 Oct 2015; revised 8 Dec 2015; accepted 22 Dec 2015; published 29 Jan 2016

Besides, detection accuracy of a sensor is the reciprocal of FWHM, i.e. $D_n = 1/FWHM$ [19]. Therefore, lower FWHM values means the sharper resonance curve resulting the higher detection accuracy. Furthermore, as depicted in Fig. 3(b), the proposed sensor shows the linearity R^2 value of 0.9432 in the sensing range of 1.46 to 1.485, which indicates the high linear sensing response. Assuming the minimum spectral resolution of $\Delta\lambda_{min}$ = 0.1 nm and considering the maximum peak shift $\Delta\lambda_{peak}$ = 115 nm, which is obtained based on the analyte RI variation of Δn_a = 0.005, as shown in Fig. 3(a), the RI resolution can be calculated as following equation [15].

$$R = \Delta n_a \times \Delta\lambda_{min} / \Delta\lambda_{peak} \text{RIU} \tag{6}$$

The resolution of the proposed sensor is as high as 4.35×10^{-6} RIU, which indicates capability of the sensor in detecting very small RI changes in the order of 10^{-6}, which is better compared to the results reported in [14, 16, 17].

The performance comparison of the proposed sensor and the previously reported SPR sensors are presented in Table 2.

Table 2. Performance comparison of the reported SPR sensors.

Structural configuration of RI sensor	RI Range	Wavelength sensitivity, nm/RIU	Amplitude Sensitivity, RIU^{-1}	Resolution (using wav. inter.), RIU	Ref.
Bragg fiber based SPR sensor	1.32-1.342	12000	269	8.3×10^{-6}	[5]
Hollow core D-shaped PCF SPR sensor	1.32-1.36	6430	N/A	N/A	[13]
Liquid core PCF based SPR sensor	1.45-1.53	–5000, 3700	N/A	2.7×10^{-6}	[14]
Multi-hole fiber based SPR sensor	1.33-1.35	2000	370	N/A	[15]
Selectively ITO coated PCF-SPR sensor	1.33-1.35	2000	N/A	5×10^{-5}	[16]
Silver-Graphene based PCF SPR sensor	1.46-1.49	3000	418	3.33×10^{-5}	[17]
Solid core D-shaped PCF SPR sensor	1.33-1.38	7300	N/A	N/A	[20]
Graphene based PCF SPR sensor	1.33-1.37	N/A	860	N/A	[21]
Selectively coated PCF SPR sensor	1.46-1.52	–4354.3, 2280	N/A	N/A	[36]
Solid core honeycomb PCF SPR sensor	1.32-1.34	13750	400	N/A	[41]
MCFF based SPR sensor	1.46-1.485	23000	820	4.35×10^{-6}	(Proposed Sensor)

The thickness of the gold layer is influential on the sensing performance as well. The effect of analyte RI and gold thickness changes on the loss spectrum are shown in Fig. 4(a). Figure 4 shows the blue shift of the loss spectrum with the increase of gold layer thickness. At thickness of t = 40 nm, the maximum losses of 697 and 723 dB/cm are achieved at resonant wavelength of 1.345 and 1.330 μm due to analyte RI of 1.460 and 1.465, respectively. The variation in Au layer thickness will affect the real n_{eff} of the surface plasmon mode, thus causing the shift in phase matching wavelength.

#252520 Received 22 Oct 2015; revised 8 Dec 2015; accepted 22 Dec 2015; published 29 Jan 2016

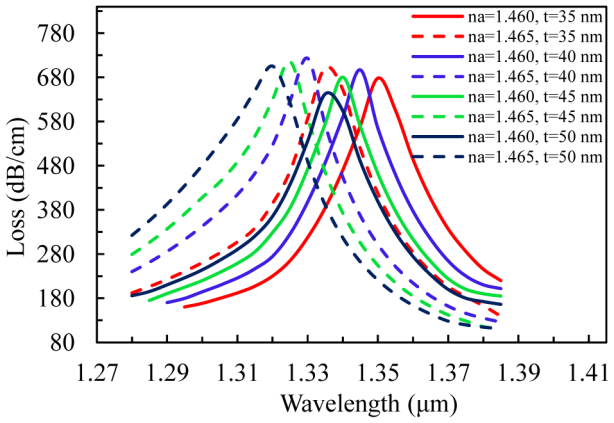

Fig. 4. Loss spectrum vs. wavelength with varying gold thickness from 35 to 50 nm; by setting $n_a = 1.46$, $d_c = 1.20\ \mu m$ and $t_t = 80$ nm.

In addition, we have observed that the loss depth of the sensor is decreased with thicker Au layer as indicated in Fig. 4. This is attributed to the lower penetration of evanescent field towards the surface with thicker Au layer. The variation in loss depth is a critical issue as it will affect the sensitivity of the sensor in amplitude interrogation mode. Practically, the thickness of the Au layer should be determined specifically for optimum sensing performance in wavelength or amplitude interrogation.

Besides the gold layer thickness, the effects of TiO_2 layer thickness on the sensing performance is investigated. TiO_2 attracts the core-guided evanescent fields towards the surface and help to facilitate the interaction between the core-guided mode and the SPP mode. Due to its high refractive index, it turns the sensor operation in near-infrared region [15]. The effect of loss spectra due to variation of TiO_2 thickness from 70 to 85 nm are shown in Fig. 5(a).

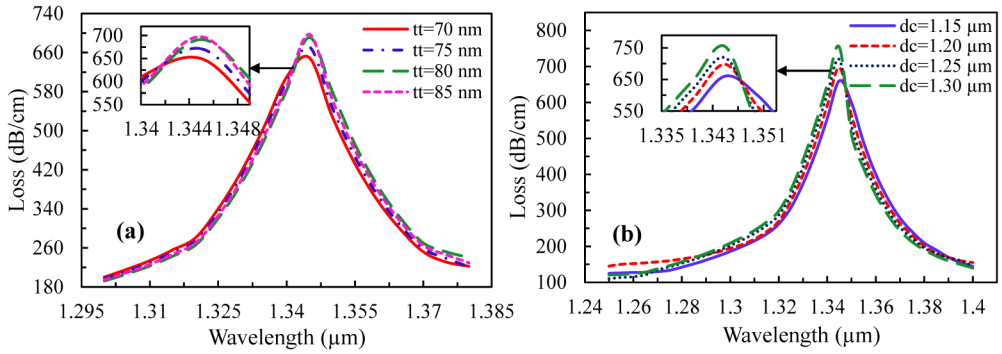

Fig. 5. Loss spectrum analysis with varying the (a) TiO_2 thickness, and (b) liquid core-diameter (d_c); setting $n_a = 1.46$, $d = 1$ μm, and $t = 40$ nm.

It is clearly observed that the loss peaks appear at 1.345 μm wavelength and the loss depths are increase slightly with the increment in TiO_2 thickness. The minimum loss value 649 dB/cm is achieved while the TiO_2 thickness is 70 nm and it increases to the maximum loss value of 697 dB/cm at the thickness of 85 nm. Due to increment of TiO_2 thickness, evanescent field is attracted towards the surface and interacts strongly with the analytes, thereby, the loss depth are gradually increased.

The core diameter effects on the sensing performance is also considered, as shown in Fig. 5(b). Due to the change of liquid-filled core diameter d_c from 1.15 to 1.30 μm, resonance peaks are found to be around 1.345 μm with very small shift toward the shorter wavelength

#252520 Received 22 Oct 2015; revised 8 Dec 2015; accepted 22 Dec 2015; published 29 Jan 2016

and slightly gaining in the resonance depths. At the core-diameter of 1.15 μm, loss value 660 dB/cm is achieved, while it is dramatically increased to 753 dB/cm when the d_c is increased to 1.30 μm. This indicates the stronger coupling between the core-guided fundamental mode and SPP mode with the increase of d_c.

Furthermore, the performance of the sensor is evaluated by the mean of amplitude detection method. Spectral manipulation is not necessary in this method as all the measurement operations are done in a specific wavelength [41]. The effect of analyte RI and gold thickness variation on amplitude sensitivity is shown in Figs. 6(a) and 6(b), respectively, considering the optimum core diameter of d_c = 1.20 μm.

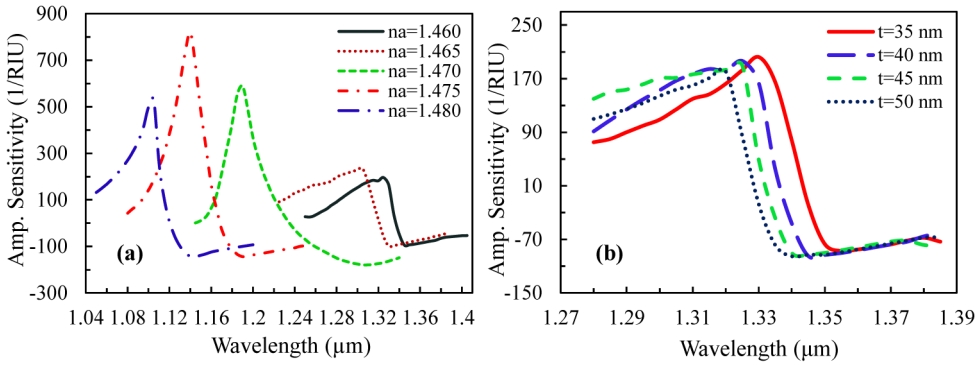

Fig. 6. Dependence of the sensor amplitude sensitivity with the variation of (a) analyte RI, and (b) gold thickness at analyte RI, n_a = 1.460.

The amplitude sensitivity can be calculated by the following equation [17].

$$S_A(\lambda)[RIU^{-1}] = -\frac{1}{\alpha(\lambda, n_a)} \frac{\partial \alpha(\lambda, n_a)}{\partial n_a} \tag{7}$$

where, $\alpha(\lambda, n_a)$ is the overall loss where RI is equal to n_a and $\partial\alpha(\lambda, n_a)$ is the loss difference of two loss spectra due two adjacent analyte RI.

As shown in Fig. 6(a), the maximum amplitude sensitivity of 820 RIU^{-1} is obtained at 1140 nm wavelength for the analyte RI n_a = 1.475. The proposed amplitude sensitivity result is comparable with the results reported in [5, 15, 21]. The proposed sensor resolution of 1.22 × 10^{-5} RIU is achieved (considering amplitude sensitivity 820 RIU^{-1}), by assuming the minimum 1% change of the transmitted intensity is detectable. Amplitude sensitivities of 196, 233, 590 and 534 RIU^{-1} are achieved for the other analyte RI of 1.46, 1.465, 1.47 and 1.48, respectively. The amplitude sensitivity is found to be inversely proportional to the gold thickness as depicted in Fig. 6(b). The maximum amplitude sensitivity achieved is 202 RIU^{-1} at 1.330 μm for the gold thickness of 35 nm. This implies the sensing resolution of 4.95 × 10^{-5} RIU with the same assumption of 1% change of the transmitted intensity. Moreover, amplitude sensitivity of 196, 190 and 181 RIU^{-1} are achieved with the gold thicknesses of 40, 45 and 50 nm, respectively. By increasing the gold thickness, sensitivity is decreased significantly, due to the higher damping loss for the thicker gold layer. Owing to the high wavelength sensitivity, amplitude sensitivity and high sensor resolution, the proposed sensor could be implemented as a standard sensor for high RI analytes detection. For experimental implementation, light source can be guided into the liquid cores of the MCFF via appropriate beam shaping by using lens or tapered lens fiber. On the other hand, multimode fiber or large numerical aperture lens can be used to collect the light from the output of MCFF and guide the light into a spectrometer or optical spectrum analyzer. Certainly, the coupling loss is not negligible due to the mode mismatching, as the coupling efficiency depends upon the modes overlap integral of the input light and MCFF. Nonetheless, we envision a delicate and efficient light multi-channels coupling by taking advantage of the hybrid format of the

#252520 Received 22 Oct 2015; revised 8 Dec 2015; accepted 22 Dec 2015; published 29 Jan 2016

proposed sensor. For instant, Y-branch or S-bend waveguide structures can be written on the flat fiber using direct UV writing techniques for efficient multi-channels butt coupling with the MCFF sensor [27]. In sum, efficient light coupling is indeed technically challenging but not fundamentally limited.

4. Conclusion

A practically simple multi-core flat fiber structure based surface plasmon resonance sensor is demonstrated for the first time. The proposed sensor shows a sensitivity as high as 23,000 nm/RIU, such sensitivity is never been reported using other microstructured SPR sensors. As the liquid-filled cores satisfy the optimum index and dispersion property simultaneously, the SPR sensing performance is increased significantly. The proposed sensor shows the average sensitivity of 9,600 nm/RIU, at the sensing RI range of 1.46-1.485. The proposed sensor shows sensing resolution as high as ~4.35×10^{-6} RIU. Additionally, the proposed sensor offers a maximum amplitude sensitivity and sensor resolution of 820 RIU^{-1} and 1.22×10^{-5} RIU, respectively. The results demonstrate the feasibility of MCFF based SPR sensor towards the possibility of integrated SPR sensor as a lab-on-a-chip for the real time diagnostic purpose.

Acknowledgments

This work is fully supported by the University of Malaya, MOHE-High Impact Research (HIR), under grant: UM.0000005/HIR.C1.

#252520 Received 22 Oct 2015; revised 8 Dec 2015; accepted 22 Dec 2015; published 29 Jan 2016